Article

Uniform Catalytic Site in Sn-β-Zeolite Determined Using X-ray Absorption Fine Structure

Simon R. Bare, Shelly D. Kelly, Wharton Sinkler, John J. Low, Frank S. Modica, Susana Valencia, Avelino Corma, and Laszlo T. Nemeth

J. Am. Chem. Soc., **2005**, 127 (37), 12924-12932• DOI: 10.1021/ja052543k • Publication Date (Web): 27 August 2005

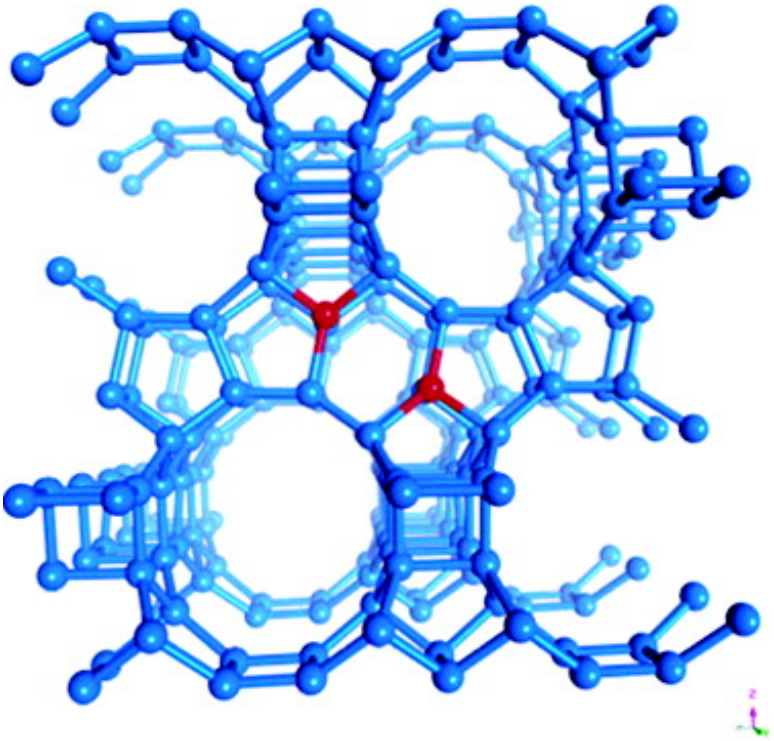

J|A|C|S
ARTICLES
Published on Web 08/27/2005

Uniform Catalytic Site in Sn-β-Zeolite Determined Using X-ray Absorption Fine Structure

Simon R. Bare,*,† Shelly D. Kelly,‡ Wharton Sinkler,† John J. Low,†
Frank S. Modica,† Susana Valencia,§ Avelino Corma,§ and Laszlo T. Nemeth*,†

Contribution from UOP LLC, Des Plaines, Illinois 60016, EXAFS Analysis, Bolingbrook, Illinois 60440, and Instituto de Tecnología Química, UPV-CSIC, Avda. De los Naranjos s/n, 46022 Valencia, Spain

Received April 19, 2005; E-mail: simon.bare@uop.com; laszlo.nemeth@uop.com

Abstract: The Sn silicate zeolite, Sn-β, has been shown to be an efficient, selective heterogeneous catalyst for Baeyer−Villiger oxidations. Using primarily a multishell fit to extended X-ray absorption fine structure (EXAFS) data, we show that the Sn does not randomly insert into the β-zeolite structure but rather occupies identical, specific, crystallographic sites. These sites are the T5/T6 sites in the six-membered rings. Moreover, the Sn is substituted in pairs on opposite sides of these six-membered rings. We believe that it is the specific, uniform crystallographic location of the Sn in the β crystal structure that leads to sites with uniform catalytic activity, and consequently to the high chemical selectivity demonstrated for this catalyst. This manifests itself in the almost enzyme-like selectivity of this catalyst in Baeyer−Villiger oxidations. This uniform site distribution of the Sn suggests that there is likely a symbiotic relationship between the structure-directing agent in the zeolite synthesis and the Sn heteroatoms during the framework formation.

Introduction

The Baeyer−Villiger (B−V) oxidation, which involves the transformation of ketones into esters or lactones, is an important reaction in synthetic organic chemistry.[1] The usual oxidants for this reaction are peracids, which are inherently unstable and lack selectivity when the organic substrate possesses reactive functional groups such as double bonds.[1] Peracids are often the choice for small-scale oxidation, but caution must be exercised when synthesis is performed at a multikilogram scale, due to the inherent instability of peracids. Recently we have reported on the use of Sn-β-zeolite as a heterogeneous chemoselective catalyst for this type of oxidation.[2−5] It was demonstrated that when 1.6 wt % Sn is incorporated into the β-zeolite crystal structure, the resulting framework substituted crystal is an efficient and stable catalyst for the B−V oxidation of saturated and unsaturated ketones by hydrogen peroxide, producing the desired lactones with >98% yield. For example, the Sn-β-catalyst yields exclusively the regioisomeric lactones in the oxidation of bicyclohept-3-en-1-one,[2] whereas when the oxidation is carried out with *m*-chloroperbenzoic acid, as is a common practice, epoxides are always produced as byproducts. High efficiency and selectivity has also been observed in many other catalytic systems (e.g. see ref 6). These earlier studies focused on the chemistry and reaction mechanism. No detailed explanation was given for the remarkable, close to 100% selectivity, in the B−V oxidation reaction achieved with the Sn-β-catalyst that has previously only been observed using monooxygenase enzymes as catalysts.[7] The selectivity of enzymes here is usually attributed to the fact that the catalytic active sites are uniform, consisting of atom(s) with specific electronic orbital orientations and specific spatial constraints. Knowledge of the precise atomic structure and chemistry of the active site, using primarily X-ray methods, has led to enormous evolution in our understanding of enzymatic catalysis.

In all zeolites, when a heteroatom is substituted for the Si or Al in the framework, the question arises as to the exact crystallographic site in the lattice where the substitution has occurred. Detailed knowledge of the site (the so-called T-sites in a zeolite) is needed for a complete understanding of the system, as the precise location of the heteroatom will affect its catalytic activity. Because this information is crucial, there have been many studies that have tried to address this issue. However, as will be discussed below, none of these studies are absolutely conclusive. This is primarily thought to be due to the difficulty in obtaining the experimental data—the heteroatom is typically substituted at only a few weight percent level in the material—and there are only a few techniques that have both the sensitivity to measure the expected changes and the ability to differentiate the heteroatom from the Si and/or Al in the zeolite framework. Two of the most studied heteroatom-substituted zeolite catalysts

† UOP LLC.
‡ EXAFS Analysis.
§ Instituto de Tecnología Química.

(1) Krow, G. R. *Org. React.* **1993**, *43*, 251.
(2) Corma, A.; Nemeth, L. T.; Renz, M.; Valencia, S. *Nature* **2001**, *412*, 423−425.
(3) Renz, M.; Blasco, T.; Corma, A.; Fornes, V.; Jensen, R.; Nemeth, L. *Chem. Eur. J.* **2002**, *8*, 4708−4716.
(4) Corma, A.; Nemeth, L. T.; Moscoso, J. G. U.S. Patent 6,344,583, 2002.
(5) Nemeth, L. T.; Corma, A.; Valencia, S.; Moscoso, S. U.S. Patent 6,191,323, 2001.
(6) Kamata, K.; Yonehara, K.; Sumida, Y.; Yamaguchi, K.; Hikichi, S.; Mizuno, N. *Science* **2003**, *300*, 964−966.
(7) Gagnon, R.; Grogan, G.; Levit, M. S.; Roberts, S. M.; Wan, P. W. H.; Wiletts, A. J. *J. Chem. Soc., Perkin Trans 1*. **1994**, *18*, 2537−2543.

10.1021/ja052543k CCC: $30.25

involve the substitution of titanium into the silicalite (MFI) framework, the so-called TS-1 catalyst, and the substitution of Fe also into MFI. The TS-1 catalyst yields remarkably high efficiency and selectivity in oxidation reactions using hydrogen peroxide,[8] while the Fe-MFI is also an active catalyst, e.g. the oxidation of benzene to phenol,[9] NO_x decomposition,[10] and conversion of methanol to light olefins.[11]

In the Ti-silicalite (TS-1) system, for example, Lamberti et al.[12] using synchrotron radiation X-ray powder diffraction (XRPD) and multiple refinement strategies concluded that there is no clear evidence of preferential substitution in any of the T-sites. Their study was aimed at using high-quality experimental data to definitively comment on prior conflicting theoretical studies[13−18] that either concluded that there was preferentially occupation of one or a few of the T-sites or that the was no clear energetic preference. Marra et al.[19] continued this work on high Ti loaded TS-1 using temperature-dependent synchrotron radiation XRPD and reported weak evidence that about half of the total Ti is located in the T10 and T11 sites of the orthorhombic unit cell, while the remaining half is spread among T1−T3 and T5−T9 and that sites T4 and T12 are not occupied by Ti. In contrast, Hijar et al.[20] used Rietveld refinement of powder neutron diffraction data, exploiting the scattering length contrast between titanium, to determine that the Ti occupies sites T3, T7, T8, T10, and T12. The following year Henry et al.[21] also using power neutron concluded that the Ti substitution is indeed nonrandom, with Ti preferentially occupying the sites T8, T3, and T10 in decreasing occupancy of Ti. In the same year, Lamberti et al.[22] also reported results using neutron powder diffraction and came to yet another conclusion. They reported strong evidence that the T6, T7, and T11 sites are the most populated, with weak evidence that there is also occupancy of Ti in T10. They also concluded that their data excluded occupancy of Ti in sites T1, T2, T4, T5, T9, and T12. However, an interesting conclusion from their work was that defective silicalite has been shown to exhibit the same preferential sites for Si vacancies, suggesting that the incorporation of Ti atoms in the MFI framework occurs via the insertion of Ti into the defective sites.[23]

In the Fe-MFI case, Milanesio et al.[24] used synchrotron XRPD to try to determine the location of the Fe^{III} in the MFI lattice. Their data provided "a rather convincing indication" of the preferential location of the Fe occupying the T9 and T10 sites. However, their results contradicted the earlier study of Hijar et al.,[20] who concluded that the Fe preferentially occupies the T8 sites. Recently Palin et al. used single-crystal synchrotron radiation XRD to probe the heteroatom distribution in B- and Ga-substituted MFI.[25] For these zeolites they concluded that a small but significant degree of preferential substitution exists, with sites T1 (and possibly T4 and T11) for B and T2 (and possibly T12) for Ga. They also commented that the site of preferential substitution may depend on the heteroatom type (size and charge). These examples clearly illustrate the difficulty associated with the determination of the T-site location of a heteroatom in the zeolite framework using PXRD or neutron scattering.

All of these studies are based either on X-ray or neutron diffraction. To our knowledge, there have been no studies where the site of substitution of the heteroatom in the zeolite has been definitively proven using extended X-ray absorption fine structure (EXAFS) spectroscopy. Lewis et al.[26] used calculations of the Fe site in MFI to better fit prior experimental EXAFS data and concluded that Fe substitution occurs over a broad range of sites, although their calculations suggested that T18 and T19 are most energetically favored. On the same system, Matsubayashi et al.[27] compared the results of FEFF calculations to experimental EXAFS data to conclude that a few of the sites are occupied by Fe. They did not attempt any fitting or modeling of their data.

In this study we report on the T-site location of Sn in β-zeolite, determined using EXAFS spectroscopy, to facilitate the understanding of the remarkable selectivity of the Sn-β-catalyst in the chemically demanding B−V oxidation reaction. At the Sn K absorption edge an s-shell photoelectron is created and then scatters from the neighboring atoms, creating interference in the absorption coefficient that reveals information about the local atomic environment of the few wt % Sn atoms in the β-zeolite lattice. There are no other techniques that can reveal similar detailed structural information around the Sn atoms in this zeolite catalyst. In particular, Rietveld refinement of powder X-ray diffraction data cannot be applied, as the β-zeolite is a highly faulted intergrowth of two polymorphs, A and B, resulting from a stacking disorder in one-dimension,[28] and the material is too electron beam sensitive for structure determination using high-resolution transmission electron microscopy (HRTEM). The recent study by Wright et al.,[29] which successfully imaged the growth defects in β-zeolite using HRTEM,

(8) Taramasso, M.; Perego, G.; Norati, B. U.S. Patent 4,410,501, 1993.
(9) Kharitonov, A. S.; Fenelonov, V. B.; Voskresenskaya, T. P.; Rudina, N. A.; Molchanov, V. V.; Plyasova, G. I. *Zeolites* **1995**, *15*, 253.
(10) Sobolev, V. I.; Panov, G. I.; Kharitonov, A. S.; Rommanikov, V. N.; Volodin, A. M.; Ione, K. G. *J. Catal*. **1993**, *139*, 435. Yogo, K.; Tanaka, S.; Ono, T.; Mikami, T.; Kikuchi, E. *Microporous Mater*. **1994**, *3*, 39.
(11) Inui, T.; matsuda, H.; Yamase, O.; Nagata, H.; Fukuda, K.; Ukawa, T.; Miyamoto, A. *J. Catal*. **1986**, *98*, 491. Handreck, G. P.; Smith, T. D. *J. Chem. Soc., Faraday Trans. 1* **1989**, *85*, 3195.
(12) Lamberti, C.; Bordiga, S.; Zecchina, A.; Carati, A.; Fitch, A. N.; Artoli, G.; Petrini, G.; Salvalaggio, M.; Marra, G. L. *J. Catal*. **1999**, *183*, 222−231.
(13) Jentys, A.; Catlow, C. R. A. *Catal. Lett*. **1993**, *22*, 251.
(14) Sastre, G.; Corma, A. *Chem. Phys. Lett*. **1999**, *302*, 447.
(15) Millini, R.; Perego, G.; Seiti, K. In *Zeolites and Related Microporous Materials: State of the Art 1994, Studies in Surface Science and Catalysis*; Elsevier: Amsterdam and New York, 1994; Vol. 84, p 2123.
(16) Oumi, Y.; Matsuba, K.; Kubo, M.; INRI, T.; Miyamoto, A. *Microporous Mater*. **1995**, *4*, 53−57.
(17) Njo, S. L.; van Koningsveld, H.; van de Graaf, B. *J. Phys. Chem. B* **1997**, *101*, 10065−10068.
(18) Ricchiardi, G.; de Man, A.; Sauer, J. *Phys. Chem. Chem. Phys*. **2000**, *2*, 2195−2204.
(19) Marra, G. L.; Artolit, G.; Fitch, A. N.; Milanesio, M.; Lamberti, C. *Microporous Mesoporous Mater*. **2000**, *40*, 85−94.
(20) Hijar, C. A.; Jacubinas, R. M.; Eckert, J.; Henson, N. J.; Hay, P. J.; Ott, K. C. *J. Phys. Chem. B* **2000**, *104*, 12157−12164.
(21) Henry, P. F.; Weller, M. T.; Wilson, C. C. *J. Phys. Chem. B* **2001**, *105*, 7452−7458.
(22) Lamberti, C.; Bordiga.; Zecchina, A.; Artoli, G.; Marra, G.; Spano, G. *J. Am. Chem. Soc*. **2001**, *123*, 2204−2212.
(23) Artoli, G.; Lamberti, C.; Marra, G. *Acta Crystallogr. Sec. B* **2000**, *B56*, 2−10.
(24) Milanesio, M.; Lamberti, C.; Aiello, R.; Testa, F.; Piana, M.; Viterbo, D. *J. Phys. Chem. B* **2000**, *104*, 9951−9953.
(25) Palin, L.; Lamberti, C.; Kvick, A.; Testa, F.; Aiello, R.; Milanesio, M.; Viterbo, D. *J. Phys. Chem. B* **2003**, *107*, 4034−4042.
(26) Lewis, D. W.; Catlow, C. R. A.; Sankar, G.; Carr, S. W. *J. Phys. Chem.* **1995**, *99*, 2377−2383.
(27) Matsubayashi, N.; Shimada, H.; Imamura, M.; Sato, T.; Okabe, K.; Yoshimura, Y.; Nishijima, A. *Catal. Today* **1996**, *29*, 273−277.
(28) Newsham, J. M.; Treacy, M. M. J.; Koetsier, W. T.; DeGruyter, C. B. *Proc. R. Soc. London A* **1988**, *420*, 375−405. Both the A and B polymorphs of β-zeolite are constructed of the same centrosymmetric building units that are arranged in layers that interconnect in either a left- (L) or right-handed (R) fashion. Polymorph A is RRRR or LLLL layers, while polymorph B has alternating RLRL stacking.
(29) Wright, P. A.; Zhou, W.; Perez-Pariente, J.; Arranz, M. *J. Am. Chem. Soc*. **2005**, *127*, 494.

noted that the zeolite is e-beam sensitive. The addition of the Sn makes the material even more e-beam sensitive, precluding such structural studies using HRTEM.

Experimental Section

Materials Preparation. Sn-β-zeolite was synthesized using the fluoride synthesis route according to procedures described in detail previously.[2,3] Briefly, Sn-β-zeolite was synthesized from tetraethyl orthosilicate (TEOS), tetraethylammonium hydroxide (TEAOH), and $SnCl_4 \cdot 5H_2O$. The mixture was stirred until ethanol formed from hydrolysis of the TEOS. HF was then added to the clear solution, and a thick paste formed. Finally, a suspension of pure silica nanocrystalline (20 nm) zeolite β seeds in water was added. The final gel composition was 100 SiO_2:X SnO_2:56 TEAOH:750 H_2O:56 HF. Crystallization was carried out for 10 days at 140 °C. The resultant material was dried and calcined.

Materials Characterization. The EXAFS data were collected at beamline 33-BM at the Advanced Photon Source, and at beamline ×18B at the National Synchrotron Light Source, both using a Si(111) double crystal monochromator. Data were recorded in transmission mode. A white beam slit of 0.3 mm was used on both beamlines. The energy was calibrated using Sn foil. The maximum of the first derivative of the absorption edge was set to 29.200 keV. The energy resolution was checked by comparing the known absorption features of the Sn foil XANES to that in the documentation accompanying the standard metal foils supplied by EXAFS Materials. The Sn K-edge EXAFS data were recorded in situ using a custom-designed reactor.[30] The zeolite powders were hand-pressed to give a uniform density sample. The sample was placed inside the in situ quartz tube reactor, which was coupled to a gas handling system. A clamshell furnace is placed around the reactor, and the temperature is controlled using a Eurotherm controller. The EXAFS data were collected at room temperature after each sample was dried in situ by heating to 525 °C at 5 °C/min in 20%O_2/80%N_2 (dried by passing though a Mat/Sen purifier) and held at 525 °C for 30 min. Multiple scans were averaged to improve the signal−noise ratio.

Data reduction and analysis were performed using the methods of Athena and Artemis.[31] The background was removed from each data set and then the resulting $\chi(k)$ data were averaged using standard procedures. The data were fit in R-space with theoretical models constructed from FEFF[32] based on the crystal structure of Sn-β.[28]

The XRD data were collected on a Scintag XDS-2000 diffractometer equipped with Peltier effect cooled solid-state detector and a Cu Kα X-ray source. Diffraction patterns were obtained in a step-scan mode in the 2θ range of 2−70°, with step size of 0.02° and counting time of 1 s/step.

The TEM samples were prepared both by dispersion of the zeolite powder suspended in ethanol onto a carbon-coated Cu grid and by embedding and sectioning. The images were collected using a JEOL 2000FX transmission electron microscope operated at 200 kV. The STEM images were collected using a VGHB601UX scanning transmission electron microscope operated at 100 kV.

Pyridine FTIR analysis was performed on a 13-mm diameter self-supporting pellet. The sample was pretreated in helium flow at 500 °C for 2 h. At the end of heating cycle, the sample was cooled to ambient temperature in helium and an FTIR spectrum was collected for hydroxyl analysis. The sample was exposed to a helium stream saturated with pyridine at 7 °C ($P/P_0 = 0.02$) at 150 °C for 1 h. The pyridine was desorbed stepwise in helium for 1 h each at 150, 300 and 450 °C, cooling to room temperature between steps. The adsorbed pyridine bands at 1550 cm^{-1} (Brönsted) and 1450 cm^{-1} (Lewis) were integrated and normalized to the sample pellet weight. The spectra were recorded on a Nicolet Magna 550 Infrared spectrometer at 2 cm^{-1} resolution, using a cooled MCT-B detector.

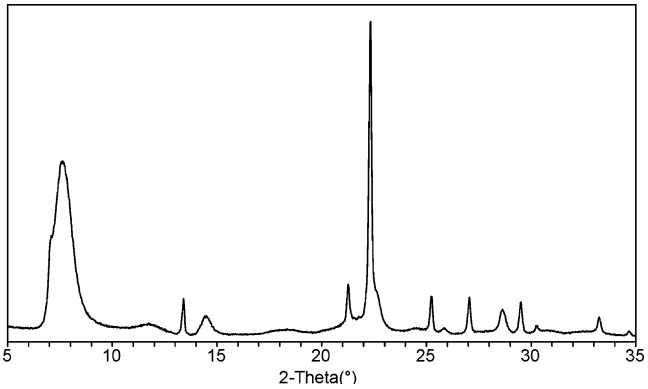

Figure 1. Powder X-ray diffraction of the calcined 1.6 wt % Sn-β-zeolite.

Table 1. Sn-β Acidity As Measured by Pyridine FTIR

	Brönsted			Lewis		
temp (°C)	150	300	450	150	300	450
integrated area/ mg zeolite	0.003	0.001	0.001	0.129	0.013	0.007

Results and Discussion

The Sn-β-zeolite, following calcination, is crystalline, consistent with the BEA-type framework topology as determined by powder X-ray diffraction (Figure 1). In particular, there are no diffraction peaks that can be attributed to a distinct cassiterite, SnO_2, phase, the expected form of any extraframework Sn material. The powder pattern is consistent with the presence of both A and B polymorphs of β-zeolite. Analysis of the powder diffraction data using DiffaX[33] shows that the sample contains 57 ± 3% of polymorph A, with the balance being polymorph B. These polymorphs of β-zeolite only differ in the way the layers are stacked; the changes in the layer sequence do not block the channels, nor change their size and dimensionality.

Table 1 shows the acid strength distribution calculated from the pyridine adsorption IR data. The distribution is broken down into weak, moderate, and strong sites. Weak sites are defined as those that retain pyridine after 150 °C desorption but not after 300 °C desorption. Moderate sites are those that retain pyridine up to 300 °C but not up to 450 °C desorption. Strong sites retain pyridine even after 450 °C desorption. The peak area/mg is reported for each type of site. This value is directly proportional to the number of sites accessible to pyridine. As expected, the pyridine-FTIR shows that the Sn-β-zeolite has essentially no measurable Brönsted acidity and only weak Lewis acidity.

Representative low-magnification micrographs obtained by transmission electron microscopy (TEM) of the sample are shown in Figure 2. The morphology of the zeolite crystals shows well-defined facets.

Examination at higher resolution shows crystals that consist of multiple domains of the two polymorphs, as expected, in agreement with the XRD data.[28] Many energy dispersive spectroscopy spectra were collected in order to determine the

(30) Bare, S. R.; Mickelson, G. E.; Modica, F. S.; Yang, N.; Ringwelski, A. Z. *Rev. Sci. Instrum.*, to be submitted.
(31) Newville, M.; Ravel., B. *J. Synchrotron Radiat.* **2005**, *12*, 537−541.
(32) Rehr, J. J.; Mustre de Leon, J.; Zabinsky, S. I.; Albers, R. C. *J. Am. Chem. Soc.* **1991**, *113*, 5135.
(33) Treacy, M. M. J.; Newsam, J. M.; Deam, M. W. *Proc. R. Soc. London A* **1991**, *433*, 499.

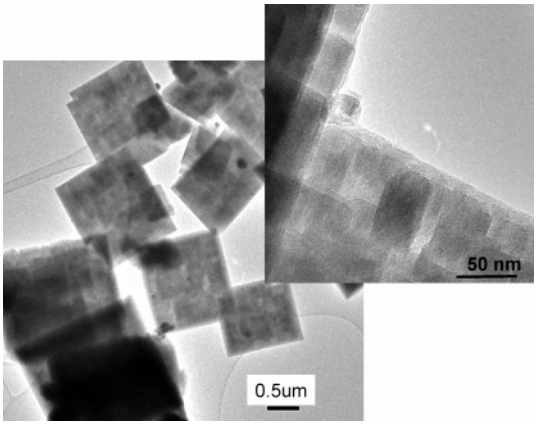

Figure 2. Low-magnification transmission electron micrographs of the calcined Sn-β-zeolite. Occasional ~1-nm Sn-rich particles can be seen decorating the edges of the zeolite crystals.

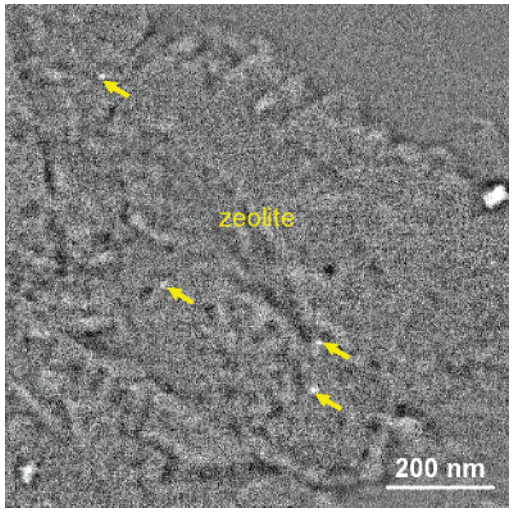

Figure 3. STEM image of microtomed Sn-β-zeolite. The STEM images are consistent with the TEM images in terms of the SnO_2 particle sizes and their number/distribution (arrows). The particles are clearly not associated with the Sn-β-zeolite. The image was processed using a high-pass filter to enhance particle contrast.

uniformity of the Sn dispersion in the β-zeolite crystal (Table S1). The data show that the Sn is homogeneously dispersed within the β-zeolite. In addition there are occasional ~1-nm-diameter Sn-rich particles. Selected-area electron diffraction is consistent with these particles being nanocrystalline cassiterite. Scanning transmission electron microscopy (STEM) (Figure 3) showed that these SnO_2 particles are not associated with the zeolite lattice. There are no discrete, Sn-rich clusters in the zeolite pores observable by STEM. Figure S1 shows elemental X-ray maps for Sn, Si, and O recorded by STEM. Thus, from the microscopy, we can conclude that, in addition to the uniform distribution of Sn incorporated in the β-crystal lattice, there is also a small amount of extraframework tin.

The raw Sn K-edge EXAFS spectra from the framework-cation-substituted β-zeolite sample together with that from cassiterite reference material are shown in Figure 4a. These spectra show the excellent data quality, extending to 16 $Å^{-1}$. The magnitude (left panel) and real part (right panel) of the Fourier transform (FT) of these EXAFS spectra are shown in Figure 4b,c.[34] The first peak in the FT of the data is shifted to lower radial distance for the Sn-β data relative to the SnO_2 spectrum. This shift in the first-shell peak distance indicates a

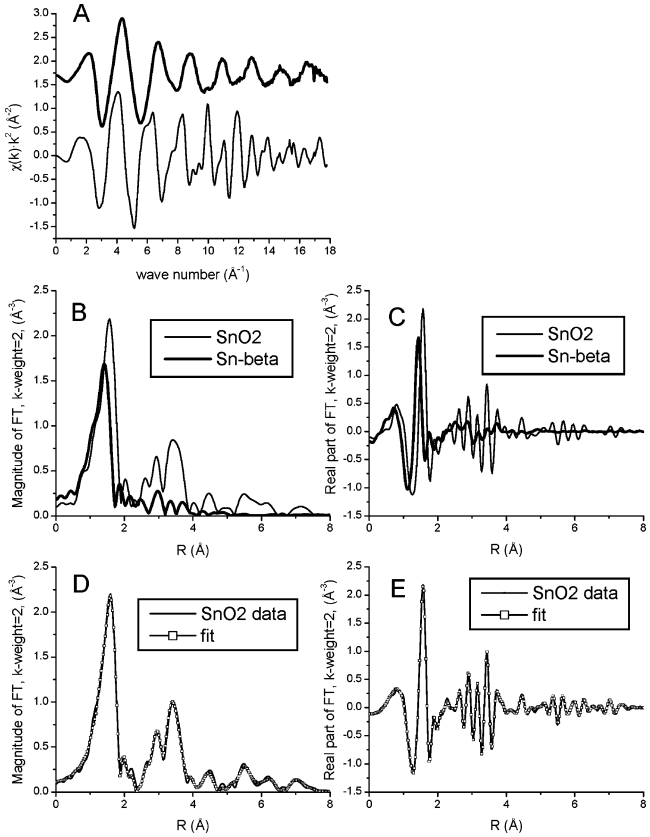

Figure 4. EXAFS data from the cassiterite (SnO_2) and Sn-β samples. (A) Comparison of the EXAFS signal ($\chi(k)\cdot k^2$) for the SnO_2 data (thin line) and Sn-β data (thick line). Comparison of the magnitude (B) and real part (C) of the Fourier transform (FT) of the SnO_2 data (thin line) and the Sn-β data (thick line). The FT data range is from 2.5 to 13.0 $Å^{-1}$ with a k-weight of 2. Magnitude (D) and real part (E) of the Fourier transform (FT) of the SnO_2 data (thin line) and model (line with symbols). The FT data range is from 2.5 to 15.8 $Å^{-1}$ with a k-weight of 2. The fit range is from 1 to 7.7 Å.

change in the first-shell oxygen distance (Sn−O) from 2.05 Å in SnO_2 to 1.91 Å in Sn-β. This is fully consistent with the change from octahedral to tetrahedral coordination, which is expected if the Sn atoms are substituted into the β crystal framework. The FT of the SnO_2 reference spectrum has an intense peak between 2.5 and 4 Å as a result of Sn−Sn scattering. This peak is also present at a very minor level in the Sn-β sample. From this initial survey of the EXAFS data it appears that the majority of the Sn atoms in the zeolite sample are substituted into the zeolite crystal framework. However, there is also a small, but nonnegligible, extraframework SnO_2 component, as there are similarities between the Sn-β and SnO_2 EXAFS data over the entire data range. In addition, the energy value for the rise in the Sn K absorption edge (29.2042 keV) indicates that the Sn is present as Sn(IV). This preliminary analysis of the EXAFS data is fully consistent with the TEM and XRD data.

Figure 4d,e shows the magnitude and real part of the FT of the bulk SnO_2 used as a reference compound. The narrow line

(34) The EXAFS spectrum is a sum of signals, each with a distinct frequency that is related to the distance between the Sn atoms and the neighboring atoms surrounding the Sn atoms in the sample. A Fourier transform (FT) of the EXAFS spectra separates the signals from each frequency, giving a peak with an amplitude related to the type and number of neighboring atoms and position related to the distance between the Sn atoms and the neighboring atoms. All the atoms with the same bond length, in a shell about the Sn atoms, are represented by a single peak in the FT of the data.

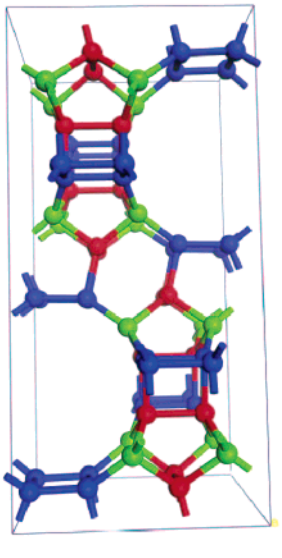

Figure 5. Schematic representation of the T sites in β-zeolite. The nine crystallographically different Si sites, designated as T1 through T9, in the β-zeolite lattice looking down the *b*-axis (for clarity the oxygen atoms are not shown). Sites T1−T4 are blue, T5 and T6 red, and T7−T9 green. Within the zeolite framework, Sn could substitute, either randomly or into specific sites, for any of the Si atoms of this structure. See also Figure S3.

is the data, and line with symbols is the fit to the data from the resulting model. Full details of the model used to fit the data are given in the Supplementary Information (Table S2 and Figure S2). The results of the excellent fit to the data from 1 to 7.7 Å are in agreement with the known bulk structure of cassiterite (Table S3).

To develop the EXAFS model in more detail, it is instructional to consider structural details of the β-zeolite. Zeolite β is a large-pore synthetic zeolite with a three-dimensional 12-ring channel system. There are two straight channels in the [100] and [010] directions and a third sinusoidal channel located parallel to the [001] direction in the A polymorph. These channels intersect, leading to a three-dimensional open-pore structure. The secondary building units consist of six-, five-, and four-membered-ring cages, each of them facing at least one side to a 12-membered-ring channel. Within this crystal structure (Figure 5) there are nine crystalographically different silicon sites, designated as T1 through T9 (Figure S2). Within the zeolite framework, Sn could substitute either randomly or into specific sites for any of the Si atoms of this structure. Figure 6 shows that the radial distribution of Si and O atoms about each of these Si sites for the pure β-zeolite structure falls into three distinct groups. Because all nine T-sites have tetrahedral coordination, each sharing an oxygen atom with the neighboring Si tetrahedra, they all have a similar atomic coordination within 0.05 Å for the first two shells of atoms. The first shell comprises four oxygen atoms at ∼1.62 Å, and the second shell four Si atoms at ∼3.15 Å. The difference between the groups of T-sites is in the orientation of the tetrahedra forming different numbers of T−O−T atom rings. On the basis of the ring structure, these sites can be readily sorted into three groups by reason of their coordination sequence.[35,36] Group I contains sites T1, T2, T3, and T4. These T-sites occupy a vertex of two 4-rings. Group II

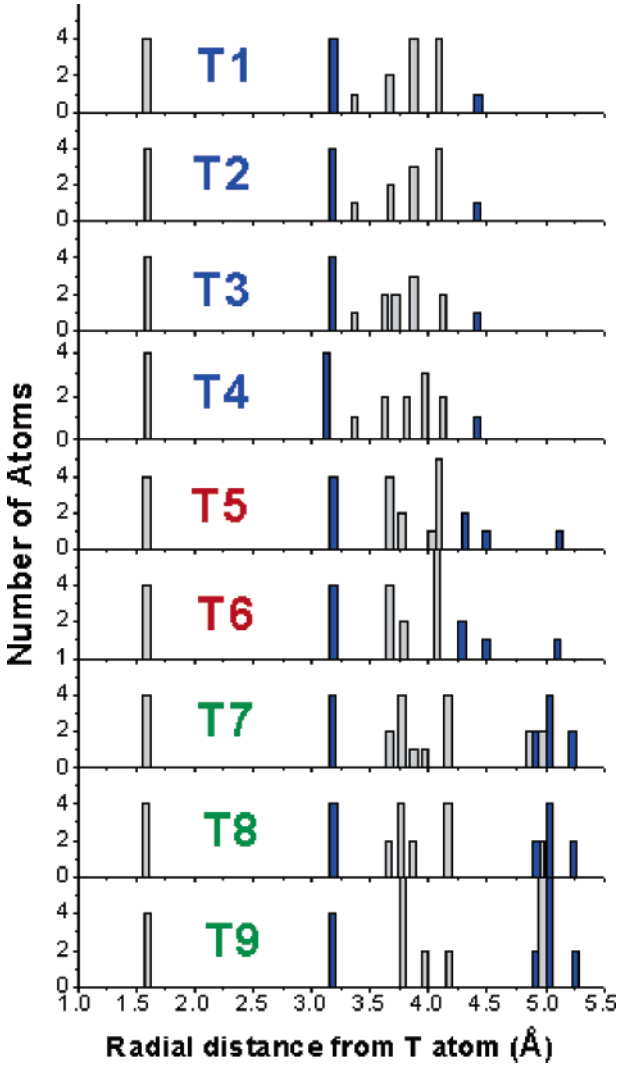

Figure 6. The radial distribution of Si and O atoms about each of the T sites for the pure β-zeolite structure. The bars (gray = O, blue = Si) depict the number and distance of the respective atoms from each T site.

contains sites T5 and T6, which occupy a vertex on a 4- and 5-ring. Group III contains sites T7, T8, and T9, which share several 5- and 6-rings. A unique property of the T5 and T6 sites is an almost linear bond from the Si atoms of the T5 site through a corner oxygen atom of the tetrahedron to the neighboring T6 site. The EXAFS signal is sensitive to collinear bonds, as the oxygen atom between the T5 and T6 site amplifies the signal; none of the other T-sites have this unique geometry. There are also large differences in the distribution of atoms in the range between 3.5 and 5.0 Å between the different groups of T-sites. At these distances the differences in the degeneracy of the Si atoms are much more important and pronounced in the EXAFS data than the O signals. Beyond the first neighboring Si tetrahedron, group I (T1−T4) is represented by one Si atom at ∼4.39 Å. Group II (T5, T6) has three shells consisting of two Si atoms at 4.28 Å, one Si atom at 4.46 Å, and one Si atom at 5.09 Å. Group III (T7−T9) is heavily weighted because of the multiple degeneracy of large membered rings about these sites, with two Si atoms at 4.88 Å, five/six Si atoms at 5.00 Å, and two Si atoms at 5.20 Å.[37] Each of these atomic distributions is EXAFS-unique. For example, the signal from five or six Si

(35) Brunner, G. O.; Laves, F. Wiss. Z. *Techn. Univsers. Dresden* **1971**, *20*, 387.
(36) Meier, W. M.; Moeck, H. J. *J. Sol. State Chem.* **1979**, *27*, 349−355.

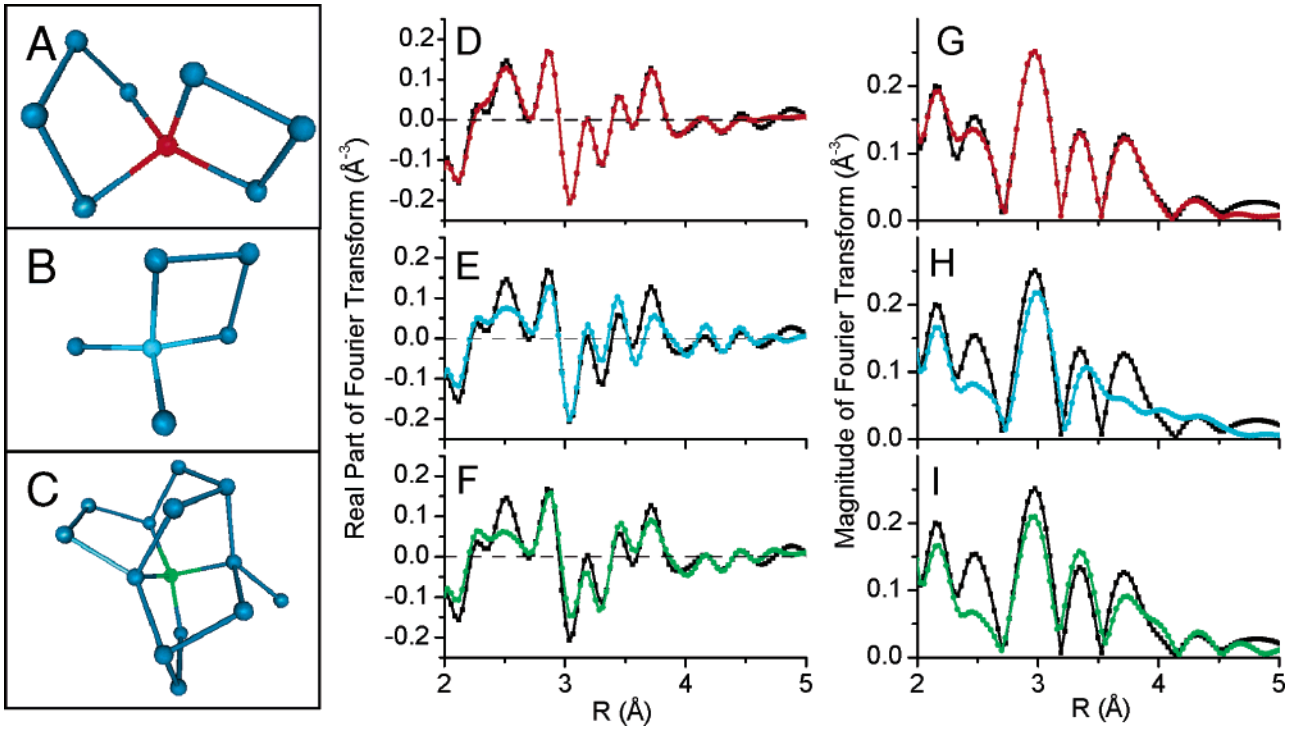

Figure 7. EXAFS fit results for Sn-β data. Each row represents one of the three possible families of sites for Sn in the β-zeolite structure. The504 schematic representations of the atoms included in the model surrounding each of these T-sites are shown in the first column (A−C). The Si atoms are represented by the blue spheres and the Sn atom (at the T-site) by the red, light blue, and green spheres for the T5 (A), T3 (B), or T9 (C) site, respectively. (The O atoms have been omitted for clarity). The T5-site is made up of a four- and a five-membered ring, the T3-site is made up of a single four-membered ring, and the T9 contains several five- and six-membered rings. The real part (D−F) and the magnitude (G−I) of the Fourier transform of the EXAFS data of the Sn-β sample are shown in the middle and final columns (black curve). Note that only the data from 2 to 5 Å are shown in D−I. The best fit data are compared to the model for Sn substitution into each of the different T-sites (red, light blue or green curves). More detailed versions of A−C with the atom types labeled and showing the O atoms are given in the Supplementary Information (Figures S4−S6).

atoms at 5.00 Å (group III) is quite different from no or one Si atom at this distance (groups I and II, respectively).

The EXAFS data are modeled by substituting a Sn atom into the β-zeolite structure at sites T3, T5, or T9. These sites are taken as representatives from each of the three distinct groups, since these sites span all the possible loop configuration of T-atoms in β. (Additional details of EXAFS models can be found in the Supplementary Information, Table S4 and Figures S4−S6). The clusters of atoms surrounding each of these sites that contribute to the EXAFS signal and the refined EXAFS model and the Sn-β data are shown in Figure 7. Note that in this figure only the EXAFS data from 2 to 5 Å is shown; otherwise, the large signal from the Sn−O first shell in the range 1−2 Å would dominate. These fits include Sn in the β-zeolite structure at site T5 (upper panel), or site T3 (middle panel) or site T9 (lower panel), together with a small fraction of the Sn atoms in the form of SnO_2.[38] The region of the FT where the models are substantially different is in the 2−5 Å range. In this range, in particular, the model for site T5 is statistically a better fit to the data than the other models. Only the model based on the T5 site can accurately account for the data. The reduced χ-squared value (χ_ν^2) of site T3 is a factor of 24 greater and that for site T9 a factor of 15 greater than that of site T5, clearly indicating that site T5 is a better model for the data.[39] In particular, the multiple scattering paths from the T5 site to the neighboring T6 site are needed to accurately reproduce the data in this region. The T3 and T9 site models underpredict the data. Thus the data show that the Sn preferentially occupies site T5 (and/or T6) in the β-crystal structure.

As the major conclusion of this work rests on the analysis of higher shell EXAFS data, where the amplitude of the signal is lower than first shell data, it is appropriate for us to show that the signal in the 2−5 Å range can be discriminated above the noise, is well-defined, and is analyzable. As stated above, the EXAFS data are dominated by the signals from the first oxygen (O1) and silicon (Si1) shells. These two signals are the same for all T1−T9 sites. It is only in the further coordination shells, in the 2−5 Å range, that there is a difference between the three unique groups of T-sites. Because our conclusions rely on the existence of a relatively small EXAFS signal, we compare the amplitude of this signal to the random fluctuations (noise) in the data. One method to accomplish this is to compare the amplitude of the signal in the FT in the range of interest to that at about 10 Å, where the signal is assumed to be dominated by noise. The noise level at 10 Å is propagated throughout *R*-space to give a feel for the uncertainty in the data relative to the amplitude of the signal. Supplemental Figure S7 shows the

(37) These distances have been rounded to the nearest hundredth angstrom and then grouped to the nearest tenth of an angstrom; therefore, an accuracy of ±0.05 Å is understood, and well within the resolution of our measurements.

(38) EXAFS data were collected on pure cassiterite to account for the minor SnO_2 component in the data analysis of the Sn-β-zeolite EXAFS data. The resulting SnO_2 model derived for the SnO_2 sample, including the scattering paths of the photoelectron and the parameters used to describe those paths, were used in the Sn-β model as a known SnO_2 signal, while the overall amplitude of the SnO_2 component was optimized in the fit to the Sn-β data to determine the percentage of total number of Sn atoms with the SnO_2 structure in the Sn-β sample.

(39) The reduced χ-squared (χ_ν^2) value for site T5 is 11, while the χ_ν^2 value for site T3 and site T9 are 266 and 167, respectively. Statistically significant changes in the χ_ν^2 value are $\sqrt{(2/\nu)} + 1 = 1.8$, where $\sqrt{(2/\nu)}$ is one standard deviation and $\nu = 18$ is the degrees of freedom in the fit.

Table 2. Best-Fit Values for the Sn-β-Zeolite Data

path[a]	N[b]	R (Å)[c]	σ^2 ($\times 10^{-3}$ Å^2)[d]
Sn−O1−Sn	4	1.906 ± 0.0001	3.1 ± 0.2
Sn−O1a−O1b−Sn triangle	12	3.252 ± 0.009	0.0 ± 0.1
Sn−Si1−Sn	3	3.499 ± 0.007	4.0 ± 0.8
Sn−O1−Si1−Sn	6	3.570 ± 0.007	4.0 ± 0.8
Sn−O1−Si1−O1−Sn	3	3.640 ± 0.007	4.0 ± 0.8
Sn−Si2−Sn	1	3.855 ± 0.096	14.9 ± 13.1
Sn−O1−Si2−Sn	2	3.876 ± 0.096	14.9 ± 13.1
Sn−O1−S12−O1−Sn	1	3.896 ± 0.096	14.9 ± 13.1
Sn−O1−Sn−O1−Sn	4	3.815 ± 0.003	12.3 ± 0.7
Sn−O2−Sn	2	4.475 ± 0.015	5.3 ± 2.0
Sn−O3−Sn	2	4.528 ± 0.015	5.3 ± 2.0
Sn−O4−Sn	2	4.626 ± 0.015	5.3 ± 2.0
Sn−Si3−Sn	3	4.033 ± 0.049	12.0 ± 5.1
Sn−Sn−Sn	1	4.992 ± 0.044	9.3 ± 4.8

[a] Path describes the scattering path of the photoelectron included in the model. For example, Sn−O1−Sn is a scattering path from the absorbing Sn atom to the first nearest oxygen atom (O1) and then back to the absorbing Sn atom. [b] N describes the degeneracy of the scattering path. For paths that include only one scattering atom, Sn−O1−Sn, N is simply the number of O1 atoms. These values were not determined in a fit to the data but taken from the crystal structure of the β zeolite. [c] R is the half-path length. For a single scattering path, this is the bond length. [d] σ^2 is the mean square displacement of the half-path length and represents the stiffness of the bond for a single scattering path. Additional parameters determined in the model include an energy shift ΔE of 0.52 ± 0.20 eV and the percent of the Sn with the nanoparticulate SnO_2 structure of 4 ± 2%, with the assumption that the remaining Sn is in the β-zeolite structure. A k-range of 2.5−13.0 Å^{-1} and an r-range from 1 to 5 Å were used, resulting in 27 independent points per data set. The model includes a total of 16 parameters. This table lists more values than parameters determined in the fit to the data because many of the values were mathematically related.

magnitude and real part of the Fourier transform of the data from 2 to 10 Å. As demonstrated in Figure S7A,B, the amplitude of the signal in the modeled data region is ~ 0.15 Å^{-3}. Figure S7C,D shows the amplitude of the signal at 10 Å is ~0.01 Å^{-3}. In fact, careful Fourier analysis shows that the signal at 10 Å is not dominated by noise but contains smooth structure representative of EXAFS signal, such that this is a generous estimate of the noise in the data. The generous noise of ~0.01 Å^{-3} is more than an order of magnitude smaller than the signal, ~0.15 Å^{-3} in the modeled region, clearly demonstrating the significant contribution of the EXAFS signal in the modeled region.

The parameters determined from the resulting best-fit model for site T5 are listed in Table 2. This fit includes a small percentage (4 ± 2%) of the total Sn being present as nonframework SnO_2 and is consistent with the (S)TEM observations. The atomic distances derived from the EXAFS data indicate that the local β-zeolite structure distorts slightly around the site of substitution, T5. A comparison of the structure for Sn at site T5 to the structure of Si at the same site is listed in Table 3. The EXAFS results indicate that the first shell of neighboring O atoms of the T5 tetrahedra are pushed away by ~16% from the Sn to accommodate the larger size of the Sn(IV) ion (0.69 Å radius in four-coordinate compounds) compared to the Si-(IV) ion (0.40 Å radius in four-coordinate compounds). Also the distance to the neighboring Si atoms that share these O atoms is expanded by 10−17%. But interestingly, the Si atoms of the next adjacent tetrahedra are closer to the Sn atom by ~7% contraction in this distance. It seems likely that these Si tetrahedra, which are on the opposite sides of the SiO_4 ring, are contracted in order to allow the four-membered ring closure.

The result, that the Sn ions within the zeolite crystal structure preferentially occupy site T5 and/or T6, led to the investigation of the spectrum derived from Sn−Sn scattering in the EXAFS

Table 3. Comparison of Site T5 in β-Zeolite As Occupied by Either a Si or a Sn Atom

path	N	R_{eff} (Å) Si in site T5a	R (Å) Sn in site T5b	ΔR (Å) % change
Sn−O1	4	1.62	1.906 ± 0.001	16
Sn−Si1	3	3.15	3.50 ± 0.01	10
Sn−Si2	1	3.20	3.86 ± 0.10	17
Sn−O2	2	3.70	4.48 ± 0.02	19
Sn−O3	2	3.75	4.53 ± 0.02	19
Sn−O4	2	3.83	4.63 ± 0.02	19
Sn−Si3	3	4.31	4.03 ± 0.05	−6.7
Sn−Sn	1	5.01	4.99 ± 0.04	−0.4

[a] Determined by XRD.[28] [b] Best fit values from this EXAFS study. The uncertainty in the percentage change is approximately 0.5% as determined from the uncertainty in the bond lengths of the EXAFS measurements. The Si tetrahedron in direct contact with the Sn tetrahedron expands, while the next nearest Si tetrahedron contracts to preserve the ring structure. The Sn−Sn distance is not affected by the substitution of the Sn atom into site T5.

data. The EXAFS model was further modified to include the first and the second T5 to T5 (or T6 to T6) distances of 4.3 and 5.1 Å, as predicted by the crystal structure of β-zeolite.[40] The results of this EXAFS modeling show a negligible contribution from the Sn atom at the 4.3 Å distance and, furthermore, that the atomic positions at 5.1 Å are 100% occupied by Sn. This gives a totally unexpected observation: the substitution of Sn into these sites is always paired. If a T5 (or T6) site is occupied by Sn, the corresponding T5 (or T6) site on the opposite side of the six-ring is always occupied by Sn. Furthermore, the EXAFS data will not accommodate a Sn atom in both of the neighboring T5 and T6 sites simultaneously. A representation of the Sn-β-zeolite structure derived from the EXAFS data is shown in Figure 8. On the basis of the amount of Sn (1.6 wt %) in the β-zeolite catalyst, the Sn loading in the sample is about 0.5 Sn atoms per unit cell (64 T-atoms). Thus, on average, only 1 out of 8 BEA unit cells is occupied by a pair of Sn atoms. We hypothesize that the distortion of the 12-membered ring (vide supra) is the limiting factor on the amount of Sn that can be accommodated into the β-zeolite framework. Additional distortion of the 12-membered rings would be required if other Sn pairs within the unit cell were filled. The EXAFS data does not reveal any information about the distribution of the Sn pairs in the BEA structure, as the distance between the pairs is too large. If the Sn substitution is random, one would expect to find pairing across the 6-ring only 6% of the time. If the Sn were randomly distributed across both T5 and T6 sites, the pairing would occur only 3% of the time. This makes the observed pairing of Sn atoms all the more remarkable. Why the Sn atoms should be paired is still not understood. It is possible that the Sn atoms may exist as dimers in the mother liquor, perhaps connected by bridging fluoride atoms, and that this could lead to pairing in the crystalline zeolite. The resulting paired Sn atoms likely provide a unique catalytic site, and it is this site that is responsible for the exceptional performance of this catalyst. Further work will be required to better understand this pairing phenomenon and its implications in the catalysis.

To further probe the uniqueness of the Sn sites in the β-zeolite two other Sn-containing silicate materials were prepared, a Sn-MCM-41 catalyst and Sn in a fully amorphous silicate (Sn-AM). The Sn level was 2 wt % in each.[41] NMR of ^{139}Sn showed

(40) These distances are the same in both polymorphs of β-zeolite.

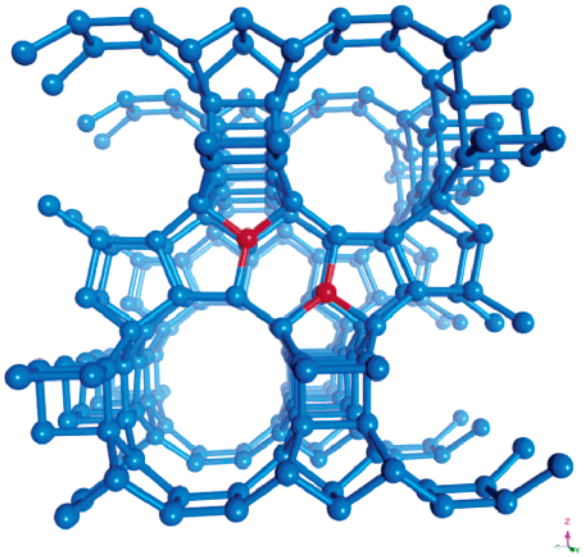

Figure 8. Representation of the Sn-β-zeolite structure as derived from the EXAFS data, viewed along the *b*-axis (for clarity the oxygen atoms are not shown). The only Sn distribution consistent with the EXAFS data is one where pairs of Sn atoms occupy opposite vertexes of the six-member rings. A pair of T5 sites (red), with the required 5.1 Å separation, is shown, representing one possible Sn-pair within the β-zeolite structure. This Sn pair distorts two of the 12-membered ring channels as viewed from the [100] direction and all four 12-membered ring channels as viewed from the [010] direction. This distortion is directed either by the replacement of Si by Sn or by the expansion of the neighboring SiO_4 tetrahedra. We speculate that the 12-membered rings will not allow additional distortion to allow another Sn pair to be filled within, on average, eight unit cells.

Table 4. Oxidation of Anisaldehyde and Cyclohaxanone with H_2O_2 and Sn-Silicates with 2 wt % Sn as SnO_2

	anisaldehyde[a]				cyclohexanone[b]	
	conv	selectivity (%)			conv	select. to
catalyst	(%)	ester	alcohol	other	(%)	lactone
Sn-AM	0.1	–	–	–	0	–
Sn-MCM-4 1	25	44	42	13	26	90
Sn-β	49	64	35	1	50	100

[a] Reaction conditions: 9 °C, dioxane solvent, anisaldehyde (3.7 mmol), H_2O_2 (5.3 mmol), 7-h reaction time. [b] Reaction conditions: 56 °C, MTBE solvent, 7-h reaction time.

that >90% of the Sn(IV) is in tetrahedral coordination. All three catalysts were tested in the oxidation of anisaldehyde and cyclohexanone with hydrogen peroxide, and the data are presented in Table 4.[41]

The results from Table 4 show that the conversion and the selectivity for oxidation of either the ketone or the aldehyde follows the order Sn-β > Sn-MCM-41 > Sn-AM. In all cases the Sn is tetrahedrally coordinated in a silicate matrix. In Sn-silicate the Sn is in a fully amorphous network of silica, and in Sn-MCM-41, the material is amorphous in the short range but possesses long range order. In Sn-β, the Sn is in a specific crystallographic position in a crystalline framework. It is only this material that exhibits the high selectivity in these oxidation reactions. Thus, we conclude that it is the framework Sn in the T5 sites that is the active Sn and not any extraframework Sn that may be present.

Electronic-structure calculations were performed in order to understand the nonrandom siting of the Sn in the β-zeolite lattice. These calculations are based on density functional theory with core-valence electron interactions represented by ultrasoft Vanderbilt pseudopotentials,[42] as implemented in VASP code.[43] We expand the one-electron wave functions in a plane-wave basis with an energy cutoff of 22 Ry. For the LDA calculation we use the Ceperley and Alder[44] exchange correlation as parametrized by Perdew and Zunger.[45] We solve the Kohn−Sham equations iteratively and optimize all atomic positions, using a conjugate gradient algorithm until the difference in energy between successive steps is <0.01 eV/Å. The unit cell volume and shape were held fixed at experimental values. Only the Γ-point was used in the *k*-point integration. Calculations were performed for one Sn atom per unit cell in the T3, T5, and T9 positions. These sites cover the groups described in the EXAFS models described above and span all the possible loop configurations of T-atoms in β-zeolite. If preferential siting of the Sn in β-zeolite is driven by thermodynamic considerations, it might be expected that the ease of substitution of the Sn^{4+} ions for Si^{4+} ions in the β-lattice would be a relevant indicator for this preference. The ability for the lattice to accommodate the Sn^{4+} ions (0.29 Å larger radius) would thus account for the preferred T site. The calculations show that Sn retains tetrahedral coordination in the β-framework with an average Sn−O bond distance of 1.885 ± 0.015 Å. This result is fully consistent the EXAFS data (1.906 ± 0.001 Å). However, there does not appear to be any correlation between the calculated substitution energies and the T5 site occupancy determined experimentally. The calculations predict the Sn prefers site T9 by 0.5 kJ/mol over site T3 and 1.7 kJ/mol over site T5.

Such small energy differences in the dehydrated zeolite are not likely to drive the distribution of Sn to any particular site during synthesis conditions. This lack of agreement for a thermodynamic rationale for the site location is in agreement with prior theoretical studies for the substitution of Ti in TS-1.[13−18] For example, Jentys and Catlow,[13] using classical potentials, predicted preferential occupancy of T6, T7, and T9 with a span of 21 kJ/mol. Sastre and Corma's[14] calculations, using a force field, favored site T8, with a range of 16 kJ/mol. Millini et al.[15] used quantum chemical methods on clusters and predicted occupancy of T4 and T10, with a range of 47 kJ/mol. Molecular dynamics (MD) calculations by Oumi et al.[16] proposed T8 as the most favorable, and a combined MD/Monte Carlo calculations by Njo et al.[17] suggested that the Ti atoms are distributed over all crystallographically different lattice sites, but that the distribution is not random, with T2 and T12 favored. Finally, Ricchiardi et al.[18] found no pronounced site preference. These computational studies are thermodynamic studies, predicting the relative energies of the heteroatom in different crystallographic sites. However, they do not take into account other factors, for example, kinetic effects that may drive the Sn (or other heteroatom) into the preferred site. These other factors include the nature of the structure-directing agent used in the synthesis and the kinetics of formation of structural precursors. The uniform site distribution of the tin in the β-lattice suggests that there is likely a symbiotic relationship between the structure-directing agent in the zeolite synthesis and the Sn heteroatoms

(41) Corma, A. Personal communication and to be published.

(42) Vanderbilt, D. *Phys. Rev. B* **1990**, *41*, 7892−7895.
(43) (a) Kresse, G.; Hafner, J. *Phys. Rev. B* **1993**, *47*, 558−561. (b) Kresse, G.; Hafner, J. *Phys. Rev. B* **1994**, *49*, 14251−14269. (c) Kresse, G.; Furthmuller, J. *Phys. Rev. B* **1996**, *54*, 11169−11186.
(44) Ceperly, D. M.; Alder, B. J. *Phys. Rev. Lett.* **1980**, *45*, 566−569.
(45) Perdew, J.; Zunger, A. *Phys. Rev. B* **1981**, *23*, 5048−5079.

during the framework formation rather than the thermodynamic stability of the resulting framework.

Summary

Our data show that the Sn does not randomly insert into the β-zeolite structure but rather occupies identical, specific crystallographic sites. These sites are the T5/T6 sites in the six-membered rings. Moreover, the Sn is substituted in pairs on opposite sides of the six-membered ring. For Sn substitution in β-zeolite, we believe that it is the specific, uniform crystallographic location of the Sn into the β-crystal structure that leads to sites with uniform catalytic activity and, consequently, to the high chemical selectivity demonstrated for this catalyst. This manifests itself in the almost enzyme-like selectivity of this catalyst in Baeyer−Villiger oxidations. This uniform site distribution of the Sn suggests that there is likely a symbiotic relationship between the structure-directing agent in the zeolite synthesis and the Sn heteroatoms during the framework formation. We continue our studies to try to resolve this issue. We believe that this work illustrates that the time is approaching when a heterogeneous catalyst can be synthesized where all of the catalytically active sites exhibit specific electronic orbital orientations and specific spatial constraints for coordinating molecules. This is achieved by ensuring that these sites are distributed in a spatially uniform manner and are accessible to reactants throughout the bulk of the solid. Consequently, these catalysts will exhibit uniform activity.

Acknowledgment. The authors thank George E. Mickelson and Natasha Erdman with help in data collection, Jennifer Wu for the DiffaX simulations, and Jule Rabo and Edith Flanigen for discussion and comments on the manuscript. The referees are thanked for their many insightful comments on the manuscript. The UNICAT facility at the Advanced Photon Source (APS) is supported by the U.S. DOE under Award No. DEFG02-91ER45439, through the Frederick Seitz Materials Research Laboratory at the University of Illinois at Urbana−Champaign, the Oak Ridge National Laboratory (U.S. DOE contract DE-A.C.05-00OR22725 with UT-Battelle LLC), the National Institute of Standards and Technology (U.S. Department of Commerce), and UOP LLC. The APS is supported by the U.S. DOE, Basic Energy Sciences, Office of Science under contract No. W-31-109-ENG-38. Research carried out (in part) at the National Synchrotron Light Source, Brookhaven National Laboratory, which is supported by the U.S. Department of Energy, Division of Materials Sciences and Division of Chemical Sciences, under Contract No. DE-A.C.02-98CH10886.

Supporting Information Available: Energy dispersive spectroscopy data from TEM, elemental X-ray maps from STEM, details of the EXAFS model, results of fitting of bulk cassiterite, and details of the EXAFS model for Sn-β-zeolite. This material is available free of charge via the Internet at http://pubs.acs.org.

JA052543K